Revisiting the Effectiveness of HCHO/NO₂ Ratios for Inferring Ozone Sensitivity to Its Precursors using High Resolution Airborne Remote Sensing Observations in a High Ozone Episode during the KORUS-AQ Campaign

Amir H. Souri[1*], Caroline R. Nowlan[1], Glenn M. Wolfe[2,3], Lok N. Lamsal[2,4], Christopher E. Chan Miller[1], Gonzalo González Abad[1], Scott J. Janz[2], Alan Fried[5], Donald R. Blake[6], Andrew J. Weinheimer[7], Glenn S. Diskin[8], Xiong Liu[1], and Kelly Chance[1]

[1]Harvard-Smithsonian Center for Astrophysics, Cambridge, MA, USA
[2]NASA Goddard Space Flight Center, Greenbelt, MD, USA
[3]University of Maryland Baltimore County, Baltimore, MD, USA
[4]University Space Research Association, Goddard Earth Sciences Technology and Research (GESTAR), Columbia, MD, U.S.
[5]Institute of Arctic & Alpine Research, University of Colorado, Boulder, CO, USA
[6]Department of Chemistry, University of California, Irvine, Irvine, CA, USA
[7]National Center for Atmospheric Research, Boulder, CO, USA
[8]NASA Langley Research Center, Hampton, VA, USA

*Corresponding Author: ahsouri@cfa.harvard.edu

Highlights:

- Ozone sensitivity over Seoul on an exceptionally degraded air quality day.
- Various thresholds for HCHO/NO₂ should be defined to label chemical regimes.
- The inherent dependence of HCHO production on NOₓ levels complicates the ratio.
- We redesign the formula to reflect the chemical feedback of NOₓ on HCHO.
- GeoTASO provides in-depth variabilities in chemical regimes over Seoul.

Abstract. The nonlinear chemical processes involved in ozone production ($P(O_3)$) have necessitated using proxy indicators to convey information about the primary dependence of $P(O_3)$ on volatile organic compounds (VOCs) or nitrogen oxides (NO_x). In particular, the ratio of remotely sensed columns of formaldehyde (HCHO) to nitrogen dioxide (NO_2) has been widely used for studying O_3 sensitivity. Previous studies found that the errors in retrievals and the incoherent relationship between the column and the near-surface concentrations are a barrier in applying the ratio in a robust way. In addition to these obstacles, we provide calculational-observational evidence, using an ensemble of 0-D photochemical box models constrained by DC-8 aircraft measurements on an ozone event during the Korea-United States Air Quality (KORUS-AQ) campaign over Seoul, to demonstrate the chemical feedback of NO_2 on the formation of HCHO is a controlling factor for the transition line between NO_x-sensitive and NO_x-saturated regimes. A fixed value (~2.7) of the ratio of the chemical loss of NO_x (LNO_x) to the chemical loss of HO_2+RO_2 (LRO_x) perceptibly differentiates the regimes. Following this value, data points with a ratio of $HCHO/NO_2$ less than 1 can be safely classified as NO_x-saturated regime, whereas points with ratios between 1 and 4 fall into one or the other regime. We attribute this mainly to the $HCHO-NO_2$ chemical relationship causing the transition line to occur at larger $HCHO/NO_2$ ratios in VOC-rich environments. We then redefine the transition line to $LNO_x/LRO_x \sim 2.7$ that accounts for the $HCHO-NO_2$ chemical relationship leading to $HCHO = 3.7 \times (NO_2 - 1.14 \times 10^{16} \text{ molec.cm}^{-2})$. Although the revised formula is locally calibrated, its mathematical format removes the need for having a wide range of thresholds used in $HCHO/NO_2$ ratios that is a result of the chemical feedback. We then use the Geostationary Trace gas and Aerosol Sensor Optimization (GeoTASO) airborne instrument to study O_3 sensitivity in Seoul. The unprecedented spatial ($250 \times 250 \text{ m}^2$) and temporal (~every two hours) resolutions of HCHO and NO_2 observations form the sensor enhance our understanding of $P(O_3)$ in Seoul; rather than providing a crude label for the entire city, more in-depth variabilities in chemical regimes are observed that should be able to inform mitigation strategies correspondingly.

Keywords: ozone sensitivity, remote sensing, formaldehyde, NO_2, emissions, modeling

Introduction

The study of ozone concentrations in the troposphere is complicated by a number of factors including the nonlinearity of the net ozone production ($P(O_3)$) to its precursor sources, primarily from nitrogen oxides (NO_x) and volatile organic compound (VOC) emissions [Sillman, 1999]. To precisely determine this complex chemical relationship, we either need to i) measure NO_x, VOC, and their chemical reactivity or ii) set up a well-established chemical

65 transport model that can fairly reproduce the relevant species abundance. The former

66 alternative is limited to spatially-sparse observations collected from campaigns and the latter

67 is too optimistic given the underlying errors associated with model inputs and mechanisms

68 [e.g., Choi and Souri, 2015a]. In absence of these models and observations, chemical proxies

69 can be used to provide some insights into the ozone-NO_x-VOC relationship. Sillman [2002]

70 validated the robustness of several proxy indicators and found H_2O_2/HNO_3 to be a solid way

71 to diagnose O_3 sensitivity. This ratio is strongly proportional to the chemical loss of HO_2+RO_2

72 (LRO_x) over the chemical loss of NO_x (LNO_x) which was revisited later in Schroeder et al.

73 [2017] who found it to be a reliable metric to locate the ridgelines in $P(O_3)$ isopleths.

74 Unfortunately, the satellite-based measurements of these two compounds are limited to scarce

75 limb soundings with limited sensitivity to the boundary layer [Mencaraglia et al., 2006;

76 Rinsland et al., 2007].

77   The absorption lines of several molecules in UV-Visible spectral range allow the

78 retrieval of HCHO [e.g., Chance et al., 1991, 1997, 2000; González Abad et al., 2015; De

79 Smedt et al., 2015], and NO_2 [e.g., Martin et al., 2002; Boersma et al., 2002; Marchenko et al.,

80 2015] from space [González Abad et al., 2019]. The availability of these observations with

81 high spatial coverage has motivated scholars to leverage HCHO and NO_2 concentrations as

82 proxies for VOC reactivity and NO_x, respectively [Tonnensen, and Dennis, 2000]. Using a

83 synergy of model simulations and the Global Ozone Monitoring Experiment (GOME)

84 HCHO/NO_2 observations, Martin et al. [2004] made an early attempt showing that surface

85 ozone production is more sensitive to NO_x than VOCs during the summers in Northern

86 Hemisphere. Duncan et al. [2010] combined models and Ozone Monitoring Instrument (OMI)

87 data to show certain ranges of HCHO/NO_2 ratios that can be useful for classifying a region into

88 NO_x-sensitive (i.e. NO_x-limited) or NO_x-saturated (i.e. VOC-limited) regimes. Following these

89 results, the ratio has been widely used for studying weekly variations in HCHO/NO_2 ratios over

90 the U.S. [Choi et al., 2012], its long term trends in Iran [Choi and Souri, 2015b], Texas [Choi

91 and Souri, 2015a], East Asia [Jin and Holloway, 2015; Souri et al., 2017], Colorado [Schroeder

92 et al., 2017; Jeon et al., 2018], and on a global scale [Jin et al., 2017]. A study of the relative

93 changes of the magnitude of the ratio in time and space is relevant; but the challenge is to

94 whether we can quantitatively rely on the absolute values to complementarily inform emission

95 regulations. A number of studies observed that differing HCHO/NO_2 thresholds differentiate

96 the transition in the chemical regimes [e.g., Schroeder et al., 2017; Jin et al., 2017]. They

97 suggested that the fuzziness in the thresholds arises mainly from the uncertainties associated

98 with the retrievals, and the variable relationship between the column and the near-surface

99   concentrations. While those sources of errors unquestionably limit the applications of column

100   HCHO/NO_2, we hypothesize that inherent dependence of HCHO production on NO_x levels

101   [Wolfe et al., 2016] can systematically result in varying HCHO/NO_2 thresholds, regardless. To

102   investigate this hypothesis, we will focus on a chemically complex city in East Asia, Seoul,

103   during the Korean-United States Air Quality (KORUS-AQ) campaign period. We will simulate

104   an ensemble of 0-D box models constrained by aircraft observations, and validate the

105   hypothesis to be able to reformulate the transition line to reflect the chemical conditions more

106   realistically.

107   The advantage of focusing on the KORUS-AQ campaign period is the availability of a

108   large suite of observations including those from airborne remote sensing [Nowlan et al., 2016;

109   Nowlan et al., 2018; Souri et al., 2018], and in situ aircraft DC-8 observations. Particularly, we

110   will use NO_2 and HCHO observations from the Geostationary Trace gas and Aerosol Sensor

111   Optimization (GeoTASO) sensor. Because of relatively small footprint, several overpasses in

112   a course of a day, solid sensor calibration, and the use of a very detailed surface bidirectional

113   reflectance distribution function (BRDF), these airborne remote sensing measurements can be

114   partly regarded as a proxy for the upcoming first geostationary satellite for monitoring air

115   pollution in the U.S. by the Tropospheric Emissions: Monitoring Pollution (TEMPO)

116   instrument [Chance et al., 2019; Zoogman et al., 2017], in East Asia by Geostationary

117   Environment Monitoring Spectrometer (GEMS, Kim et al., 2019), and in Europe by the

118   Sentinel-4 mission [Ingmann et al., 2012]. Using the airborne observations will allow us to

119   understand to what extent we can classify the chemical conditions regimes by taking into

120   account the reformulated transition line.

121   **GeoTASO**

122   Hyperspectral airborne images in the ultraviolet-visible spectrophotometry range 290

123   nm to 695 nm were captured by two 2-D CCD detector arrays using the Geostationary Trace

124   gas and Aerosol Sensor Optimization (GeoTASO) instrument [Leitch et al., 2014]. The sensor

125   was mounted on-board NASA's B200 aircraft flying at ~9 km altitude above sea level. A more

126   detailed description of the engineering configuration for this sensor can be found in Nowlan et

127   al. [2016]. Similar to other remotely sensed instruments, the size of the footprint is a function

128   of sensor geometry, aperture, aircraft speed, altitude, and targeted signal-to-noise ratios. The

129   synergy of all this factors resulted in a 250×250 m^2 spatial resolution which is ~300 times as

130   fine as that of the TROPOspheric Monitoring Instrument (TROPOMI) nadir pixels. A major

131   improvement in the sensor design compared to its former campaigns was a mirror replacement.

132 This change led to mitigating stray light in the UV range, allowing for achieving a more robust

133 retrieval.

134 The HCHO retrieval algorithm follows a conventional 2-step procedure: i) HCHO slant

135 column is retrieved via direct non-linear least-squares fitting of a GeoTASO radiance spectrum

136 (328.5 nm- 356.5 nm) taking into consideration wavelength registration, slit function

137 calibration, under-sampling, closure polynomials that represent low frequency effects of

138 aerosols and molecular scattering, interference molecules (e.g., O_3 and NO_2), and rotational

139 Raman scattering [Chance et al., 2000; Nowlan et al., 2016; 2018], ii) HCHO vertical column

140 is obtained by applying an air mass factor (AMFs) to each observation quantifying the light

141 path through a simulated atmosphere using VLIDORT [Nowlan et al., 2016; 2018]. The first

142 step requires a reference spectrum as a function of cross-track position, which is determined

143 from spectra collected over a relatively clean region in the Taebaek Mountains on 25 May. The

144 earthshine reference is preferred to a solar one because it permits more efficient removal of

145 cross-track striping and biases [Nowlan et al., 2016; 2018]. The details of the retrieval and

146 possible source of uncertainty for this product can be found in Nowlan et al. [2016]. The

147 projected fitting uncertainty on the vertical column is found on average to be 3.53×10^{15}

148 molec.cm^{-2} in our case study.

149 The NO_2 retrieval follows the similar procedure done for HCHO, but with a different

150 fitting window (425-460 nm) using the Differential Optical Absorption Spectroscopy (DOAS)

151 technique. NO_2 vertical column density (VCD) data below the aircraft using the algorithm

152 discussed in detail in Lamsal et al. [2017], with additional improvement for identification of a

153 relatively pollution free reference location for the spectral fitting process by analyzing Pandora

154 NO_2 observations at Songchon on 20 May, and proper accounting of NO_2 amount over the

155 reference location. To convert the differential slant column densities (dSCDs) from the DOAS

156 fit to VCDs, AMFs are calculated using the on-line radiative transfer calculation from

157 VLIDORT. Inputs to the AMF calculation include the solar and observation geometry, high-

158 resolution (1 km) Moderate Resolution Imaging Spectroradiometer (MODIS) BRDF [Schaaf

159 et al., 2011] to provide an intrinsic characterization of surface anisotropy, and diurnally-varying

160 NO_2 vertical profiles from a regional model constrained by OMI-derived NO_x emissions

161 [Goldberg et al., 2019]. The latter two are spatially interpolated to the GeoTASO footprint.

162 Other details on the retrievals and their uncertainties can be found in Lamsal et al. [2017]. For

163 both data we consider only cloud-free pixels using cloud flags provided in the data.

164 **An Ensemble of Photochemical Box Models**

165   In order to calculate the chemical reaction rates of several species, we use the

166   Framework for 0-D Atmospheric Modeling (F0AM) v3.1 [Wolfe et al., 2016]. The chemical

167   mechanism deployed for the calculation is based on CB6r2 [Hildebrandt Ruiz and Yarwood,

168   2013] which includes more than 77 species and 216 chemical reactions. We use observations

169   available on the DC8 platform for constraining the model by holding their values constant

170   throughout model step. This includes the required meteorological variables, photolysis

171   frequencies, and concentrations of various compounds. The averaging time for the observations

172   is 10 s. Table 1 lists inputs and configurations used for the model. Since the target of this study

173   focuses on the well-mixed boundary layer, we only incorporate those observations that are

174   within this layer based on the study of Sullivan et al. [2019]. Therefore, we limit our study to

175   afternoon only times, as the aircraft did not fly low enough during the morning. In about 15%

176   of cases, we observe missing values in some compounds (VOC-speciated gases sampling have

177   different temporal resolutions). Accordingly, we fill the missing values using linear

178   interpolation. For each sample, we assume that rapidly cycling species are in a diel steady state

179   indicating that the loss and production of most of the reactive species are in balance. To be able

180   to fulfill our assumption, we run the box model for five solar cycles consecutively. It is worth

181   mentioning that the steady state assumption may not be valid if the air parcel is in the proximity

182   of high emitters [Thornton et al., 2002]. The model integration time for each solar cycle is set

183   to 30 min. To prevent the long-lived species from accumulating over time (due to the lack of

184   transport and deposition components in the box model), we use a dilution constant equal to a

185   24-h lifetime.

186   To account for measurement random noises, we perform the simulation in a stochastic

187   framework. Accordingly, in this study, the framework of the box modeling is based on an

188   ensemble model ($R_i : i = 1, 2, \ldots, k$) with 50 members ($k$=50) generated by applying

189   randomness to the chemical compounds used for constraining the model. We focus on only

190   perturbing the gas concentrations to generate the ensemble models. The randomness

191   coefficients applied to each compound are drawn from a lognormal distribution with a mean

192   of 1, and a variance equal to the measurement precision listed in Table 1.

193   One can calculate the mean ($\overline{R}$) and covariance (P) of the reaction rates from an

194   ensemble of the box models:

$$\overline{R} = \frac{1}{k}\sum_{i=1}^{k} R_i \qquad\qquad (1)$$

$$P = \frac{1}{k-1}\sum_{i=1}^{k}(R_i - \overline{R})(R_i - \overline{R})^T \quad (2)$$

$$= \frac{1}{k-1} \boldsymbol{R} \boldsymbol{R}^T, \text{ where } \boldsymbol{R} \text{ is the vector of } \boldsymbol{R}_i - \overline{\boldsymbol{R}} \text{ (i.e., perturbations)}$$

195 Therefore, we are able to estimate a distribution for a number of variables including net ozone

196 production ($P(O_3)$), LRO_x, LNO_x, and VOC reactivity (VOCR) rates. We calculate $P(O_3)$ by

197 subtracting ozone loss mainly controlled by HO_x ($HO+HO_2$), the formation of HNO_3, and O_3

198 photolysis followed by the reaction of $O(^1D)$ with water vapor from ozone formation (through

199 removal of NO via HO_2 and RO_2) [Kleinman, 2005]:

$$\begin{aligned}
P(O_3) = {} & k_{HO_2+NO}[HO_2][NO] + \sum k_{RO_{2i}+NO}[RO_{2i}][NO] \\
& - k_{OH+NO_2+M}[OH][NO_2][M] - P(RONO_2) \\
& - k_{HO_2+O_3}[HO_2][O_3] - k_{OH+O_3}[OH][O_3] \\
& - k_{O(^1D)+H_2O}[O(^1D)][H_2O] - L(O_3 + alkenes)
\end{aligned} \tag{3}$$

200 VOCR is calculated as the sum of the product of the rate constants of VOC+OH reactions

201 ($k_{i,OH}$) and VOC concentration:

$$VOCR = \sum_i k_{i,OH+VOC_i}[VOC_i] \tag{4}$$

202 LRO_x is defined through the sum of primarily radical-radical reactions:

$$\begin{aligned}
LRO_x = {} & k_{HO_2+HO_2}[HO_2]^2 + \sum k_{RO_{2i}+HO_2}[RO_{2i}][HO_2] \\
& + \sum k_{RO_{2i}+RO_{2i}}[RO_{2i}]^2
\end{aligned} \tag{5}$$

203 LNO_x mainly occurs via the NO_2+OH reaction:

$$LNO_x = k_{OH+NO_2+M}[OH][NO_2][M] \tag{6}$$

204 Figure 1 demonstrates important interactions involved in the formation of tropospheric

205 ozone. Per one RO_x cycle (in the center of diagram), two molecules of ozone are generated.

206 The availability of NO_2 and VOC concentrations dictates the controlling factor for driving the

207 cycle. Assuming NO_x>>VOC leads to the removal of OH and NO_2 from the system (LNO_x)

208 making $P(O_3)$ a function of VOC (NO_x-saturated). On the other hand, an environment with a

209 NO_x<<VOC undergoes a change by which it loses HO_2 and RO_2 (LRO_x) molecules rendering

210 $P(O_3)$ dependent on NO_x concentrations (NO_x-sensitive). Hence, the ratio of LNO_x to LRO_x

211 offers a way to separate these two chemical condition regimes.

212 **WRF-CMAQ**

213 We simulate the atmospheric composition in East Asia using the CMAQ model [Byun

214 and Schere, 2006] at 27 km spatial resolution with 328×323 grid size. We choose the CB05

215 gas-phase mechanism and the six-generation aerosol mechanism (AERO6). The location of

216   this domain is shown in Figure 2. We process anthropogenic emissions for the CMAQ domain

217   from the MIX emissions inventory 2010 [Li et al., 2015], which contains gridded ($0.25° \times 0.25°$)

218   monthly emissions for black carbon, carbon monoxide (CO), carbon dioxide (CO_2), NO_x,

219   ammonia (NH_3), organic carbon (OC), fine and coarse particulate matter (PM2.5 and PM10),

220   sulfur dioxide (SO_2), and NMVOC in the CB05 mechanism. A diurnal factor adopted from the

221   EPA NEI2011 emissions is applied for the mobile sector. The FINN v1.6 emissions

222   [Wiedinmyer et al., 2011] are extended to include biomass burning emissions with

223   consideration of a plume height assumption commonly used in the GEOS-Chem model. For

224   biogenic emissions, we use a standalone MEGAN (v2.1) [Guenther et al., 2006] model

225   (offline), which incorporates a dynamic leaf area index from MODIS, a comprehensive

226   climatology of plant functional maps (PFT) [Ke et al., 2012], and meteorological fields from

227   the following weather model. In order to simulate the mesoscale meteorology, we use the

228   Weather Research and Forecasting model (WRF) v3.9.1 [Skamarock et al., 2008]. The

229   domain's grid is 342 steps west-east, 337 steps south-north, and 28 vertical pressure sigma

230   levels. We use the ACM2 scheme [Pleim, 2007] for the planetary layer fluxes, Kain-Fritsch for

231   cumulus parameterization [Kain, 2004], the WRF Single-Moment (WSM) 6-class scheme for

232   microphysics [Hong and Lim, 2006], Noah Land-Surface Model for the surface physics [Chen

233   and Dudhia, 2001], and Rapid Radiative Transfer Model (RRTM) for short- and long-wave

234   radiation. We account for the horizontal turbulent diffusion based on the standard Smagorinsky

235   first-order closure. The lateral boundary conditions and the grid nudging inputs come from the

236   global Final (FNL) $0.25°$ resolution model. The diurnally lateral chemical conditions are

237   generated by GEOS-Chem v10 [Bey et al., 2001] with the full chemistry mechanism (NO_x-O_x-

238   HC-Aer-Br) spun up for a year.

239   **Case Description**

240   Between April and June 2016, a joint team of researchers from the U.S. and South

241   Korea conducted an atmospheric chemistry field campaign over the Korean Peninsula and

242   surrounding open waters [https://espo.nasa.gov/korus-aq, last access: 22 June 2019)].

243   Observations were collected from a variety of observing systems encompassing surface sites,

244   airborne remote sensing, and in-situ aircraft observations. Figure 3 shows contour maps of

245   simulated surface ozone concentrations overlapped by 500 mb geopotential heights and 700

246   mb wind vectors in East Asia during the June 7th-10th 2016 period. A low pressure system aloft

247   over the very northern part of China associated with the trough (purple line) is responsible for

248   carrying on the continental polluted air masses from the west while obstructing those from

249   clean maritime regions coming from the south. In addition, the development of an

250 atmospherically stagnant condition over the North China Plain and the Yellow Sea from June

251 8th till June 9th 2016, evident in the expansion of the isobars, resulted in elevated ozone

252 concentrations over East Asia. For instance, ozone levels within the first 2 km altitude on June

253 9th 2016 around the Seoul metropolitan area are found to be 107±14 ppbv [Figure S1]. By virtue

254 of the favorable atmospheric conditions for the formation of ozone, and the availability of

255 qualified GeoTASO and DC8 observations on June 9th 2016, we focused our study on this

256 ozone episode day. It is worth noting that on any other day during the campaign, the

257 coincidence of GeoTASO and DC8 measurements was suitable to draw statistically significant

258 conclusions on the relationship between $P(O_3)$ and ozone precursors.

Ozone chemistry analysis during the episode — DC8

260 Prior to assessing the usefulness of GeoTASO at pinpointing the sensitivity of ozone to

261 its precursors, we find it essential to study the relevant chemical rates at which ozone is being

262 formed/removed. We first validate the performance of the ensemble of box models by

263 comparing OH and HO_2 measurements to the simulated values, and those from NASA Langley

264 Research Center (LaRC) box model (https://www-air.larc.nasa.gov/cgi-bin/ArcView/korusaq,

265 Last access: Dec 2019). Comparing to the observations, we observe a reasonable performance

266 in our box model with respect to correlation and bias for OH (R^2=0.43, +27%) and HO_2

267 (R^2=0.71, -20%). Moreover, both box models agree well within 10% and 34% range in terms

268 of OH and HO_2, respectively [Figure S2 and S3]. Figure 4 shows the DC-8 measurements of

269 NO_2, HCHO, O_3 below 2 km, and the simulated VOCR from the box model on June 9th 2016

270 afternoon (1400-1600 LST). The borders are administration subdivisions. The rough threshold

271 of mixing layer height is derived from ceilometer backscatter profiles shown in Sullivan et al.

272 [2019]. The altitude of the aircraft is demonstrated in Figure S4. To gather a better qualitative

273 picture of the spatial variations in NO_2 and HCHO, we plot their vertical columns observed by

274 GeoTASO in the background. We find a fair correlation (R^2=0.47 for HCHO, and R^2=0.69 for

275 NO_2) between the collocated pixels and the DC-8 measurements within a 500 m radius.

276 Not surprisingly, high concentrations of NO_2 are seen in the city mainly due to

277 anthropogenic NO_x emissions. The MIX-Asia 2010 emissions inventory suggest that the

278 primary source of NO_x emissions in the Seoul metropolitan area is the mobile sector (67%, 74

279 ton/day) followed by the residential (22%, 21 ton/day) (not shown). The measured NO_2

280 columns pinned to the city are exceptionally high (~3.1 DU = 8.3×10^{16} molec.cm^{-2}) such that

281 Pandora ground-based NO_2 column observations located in Yonsei University (Seoul) from

282 16th May to 11th June 2016 only observed such a value or higher with less than 1% occurrence

283 [Herman et al., 2018].

The retrieval of HCHO has intrinsically been difficult primarily due to the weaker molecular absorption which leads to a relatively higher detection limit and nosier values [Chance et al., 1991, 2000]. As a result, former studies mapping HCHO values on urban scales using satellite observations had to oversample years of data at a cost of losing temporal information [Zhu et al., 2014; Souri et al., 2017; Zhu et al., 2018]. The uniqueness of GeoTASO lies in its capability to observe elevated HCHO values at sub-urban scales with just one overpass [Nowlan et al., 2016], as seen in Figure 4. Souri et al. [2017] calculated the average total HCHO columns from the Ozone Monitoring Instrument (OMI) in 2005-2014 and found them to be comparatively high over Seoul, possibly a result of anthropogenic emissions. Similarly, the combination of GeoTASO and DC-8 observations reveals a pronounced level of HCHO in the urban area. A myriad of VOC compounds with various emissions sources can contribute to the formation of HCHO [Seinfield and Pandis, 2016]. A comprehensive source apportionment study using VOC measurements in Seoul during the years of 2013-2015 suggested that the major contributor to VOC concentrations were from the solvent use and mobile emissions [Song et al., 2019]. Likewise, the DC-8 aircraft measure high concentrations of ethane, ethene, and methanol in the proximity of the city, all of which are largely utilized in vehicle fuels [Figure S5-S7]. High toluene concentrations (a major product from solvent use) are mostly observed in the southern part of the city (> 5 ppbv) [Figure S8]. As another major source of VOC (and HCHO), we find high concentrations of isoprene (0.74 ± 0.23 ppbv) over Seoul (Olympic Park) [Figure S9].

A major assumption in using HCHO/NO_2 ratio for gaining some insights into ozone formation is that HCHO is a proxy for total VOCR [Duncan et al., 2010]. To reassess this assumption, we plot the DC-8 HCHO versus the simulated VOCR values on June 9th 2016 afternoon (1400-1600 LST) in Figure 5. A significant coefficient of determination (R^2=0.90) is found between DC-8 HCHO levels and the logarithm-transformed VOCR. The logarithmic dependence indicates that two quantities begin to diverge at high values. For example, the Pearson correlation coefficient between VOCR and HCHO changes from 0.9 for VOCR below 4 s^{-1} to 0.6 for VOCR above 4 s^{-1}. This drift is in agreement with Valin et al. [2016] who found that HCHO levels under high VOCR (>8 s^{-1}) are primarily dependent on OH concentrations rather than VOCR at midday (see Eq1 in the paper). Therefore, the assumption of HCHO being a proxy for VOCR might not hold for VOC-rich environments.

A second assumption in using the ratio is that it might be a proxy for the magnitude of LNO_x/LRO_x ratios [Duncan et al., 2010; Schroeder et al., 2017]. Figure 6 depicts the

relationship between the measured ratios versus the modeled LNO_x/LRO_x. Both quantities are transformed logarithmically. A high degree of negative correlation between the two variables ($R^2=0.96$) underscores the relevance of $HCHO/NO_2$ ratios to LNO_x/LRO_x values. Kleinman et al., [2001] and Kleinman, [2005] found that $P(O_3)$ is proportional to VOCR for those LNO_x/LRO_x ratios near to 1 or higher (i.e., NO_x-saturated), while for lower values, it becomes independent of VOCR (i.e., NO_x-sensitive). Schroeder et al. [2017] further reassessed this indictor (i.e. LNO_x/LRO_x) during the Colorado DISCOVER-AQ campaign and found out the LNO_x/LRO_x cut-off value should be increased to ~2.8 to correctly locate the $P(O_3)$ turnaround point mainly due to the inclusion of NO_z in their box model calculation. Assuming a NO_x/VOC transition at $LNO_x/LRO_x =1$, the fitted curve in Figure 6 suggests that the transition occurs at a $HCHO/NO_2$ ratio close to 2.8, while considering $LNO_x/LRO_x=2.8$ leads to the ratio ~1.8. We will investigate the dependency of $P(O_3)$ on $HCHO/NO_2$ ratios later.

In general, the observed ambient ozone concentrations neither correlate with HCHO nor NO_2, as they are influenced by a combination of a non-linear chemistry, dry deposition, background values, photochemistry, meteorology and stratosphere-troposphere exchange [Cooper et al., 2012]. To elucidate the chemistry, we plot the major loss and formation pathways in $P(O_3)$ calculated from the box model in Figure 7. In the presence of both relatively high VOCR rates and NO_x concentrations, we observe several ozone production hot spots through the reactions of HO_2+NO and RO_2+NO over the downtown and the downwind area (the predominant surface wind is weak northwesterly). The major pathway of chemical ozone loss in the city is through the formation of HNO_3. O_3 photolysis by the reaction of $O(^1D)+H_2O$ is the second factor for the photochemical ozone loss. The mean $P(O_3)$ is estimated at 7.66 ± 2.52 ppbv hr^{-1} with a maximum value up to 14.41 ppbv hr^{-1}. The elevated $P(O_3)$ is majorly observed over areas in which we see simultaneously high concentrations of HCHO (from isoprene) and NO_2 [Sullivan et al., 2019].

To shed light on the dependency of $P(O_3)$ on its major precursors (i.e., NO_x and VOCs), we conduct two experiments; the first experiment follows an observationally stand-alone framework involving the comparison of observed NO concentrations from DC-8 with $P(O_3)$. Such an experiment is limited to the range of observed values, thus to be able to extrapolate the analysis, the second experiment makes use of the constrained box model changing the concentrations of NO and VOCs. Here, we detach the model from the HCHO constraint to allow it to respond to changes in the primary VOCs. To perturb the values, we use a linear factor stretching from 0.1 to 15 with a 0.1 step (150 values). We apply this factor to all constrained VOCs and NO_x (excluding HCHO and aromatic VOCs) to be able to create a

351 150×150 grid in NO_2-HCHO space.

352   Figure 8 (left panel) demonstrates the relationship between the logarithm-transformed
353 NO and $P(O_3)$ colored by various VOCR rates for observations further than 50 km from Seoul
354 on the same day (mainly rural). The $P(O_3)$ values increase monotonically for all ranges of NO
355 illustrated by a high degree of correlation between them. The increases in $P(O_3)$ relative to NO
356 are steeper for larger VOCR rates. The right panel in Figure 8 shows the same relationship but
357 for those observations closer to the city (<50 km); we find that the $P(O_3)$ dependence on NO
358 follows a quadratic function. The $P(O_3)$ values increase for NO<~1 ppbv, but slow down
359 afterward. Theoretically, the location of the $P(O_3)$ turnover point depends on VOCR mainly
360 due the fact that a high reactive VOC yields a larger amount of RO_2 to react with NO [e.g.,
361 Schroeder et al., 2017]. Under high NO concentrations (a typical urban setting), air parcels
362 with high VOCR are usually associated with ample RO_2 or HO_2 molecules which enhance the
363 conversion of NO to NO_2, whereas in a low VOCR environment the radical termination
364 becomes prominent removing NO_2 from the cycle. To some extent, we observe the same
365 tendency in Figure 8, but the number of observations (over Seoul) is not adequate to statistically
366 associate the sensitivity of $P(O_3)$ with NO given a certain VOCR rate. A striking difference
367 between the two sets of observations is having much more variability for observations close to
368 Seoul, which in turn, results in increased uncertainty in the maxima (1.2-2.46 ppbv for NO).
369 This indicates the presence of diverse emissions sources, and more complex chemical condition
370 regimes, making necessary performing the second experiment for expanding our data.

371   We next explore the $P(O_3)$ isopleths as a function of HCHO and NO_2 concentrations
372 based on the average of all perturbed observations located in the proximity of Seoul (<50 km)
373 on June 9th (1400-1600 LST) (Figure 9). We furthermore overplot the associated LNO_x/LRO_x
374 isopleths (purple lines). The chemical transition point is found at LNO_x/LRO_x~2.7 which is in
375 strong agreement with those values reported in Schroeder et al. [2017]. At points on the right
376 side of this line, $P(O_3)$ mostly is a function of HCHO, thus reducing VOCs turns out to be a
377 practical way to reduce $P(O_3)$. In contrast, moving toward the left side of the line renders $P(O_3)$
378 dependent on NO_x concentrations. The LNO_x/LRO_x contours also hint about the relationship
379 between HCHO-NO_2-O_3. Enhancement of NO_2 concentrations leads to an exponential increase
380 in LNO_x/LRO_x, evident in the smaller changes in the x-intercepts of the LNO_x/LRO_x lines.
381 This is essentially due to that fact that the relationship between NO_x emissions and NO_2
382 concentrations changes from a linear form to an exponential one [Souri et al., 2017] mainly
383 because of the feedback of NO_x on its own lifetime. Another distinct feature is that the slope
384 of the LNO_x/LRO_x lines becomes less steeper as NO_2 concentrations increase. Under rich VOC

385   environments, the LNO_x/LRO_x ratios seem to be more buffering with respect to NO_2 changes.

386   A possible explanation for this tendency can be due to the $HCHO$-NO_2 relationship [Wolfe et

387   al., 2016; Chan Miller et al., 2017].

388   Martin et al. [2004] suggested that the transition between VOC-sensitive and NO_x-

389   sensitive regimes occurs at a $HCHO/NO_2$ ratio of 1. Figure 9 shows that the majority of data

390   points can safely be described as NO_x-saturated as long as $HCHO/NO_2$ is lower than 1. On the

391   contrary, any data point that results in a larger value than 1 may fall into either NO_x-sensitive

392   or NO_x-saturated regime. Duncan et al. [2010] defined an ambiguous region ranging from 1-2

393   and classified NO_x-sensitive regimes if $HCHO/NO_2 > 2$. According to Figure 9, using this

394   threshold, we would misclassify a sizable proportion of the data. We observe that the

395   discrepancy between the $HCHO/NO_2 = 2$ line and that of $LNO_x/LRO_x = 2.7$ is larger for VOC

396   rich environments. In fact, to stay on $LNO_x/LRO_x = 2.7$, $HCHO/NO_2$ can have a wide extent of

397   values ranging from 1 to 4, questioning the robustness of this indicator to ascribing the

398   chemical condition regimes. Using observations measured in DISCOVER-AQ Colorado,

399   Schroeder et al. [2017] similarly discovered that a broad range of column $HCHO/NO_2$ ratios

400   between 1.1 and 3.3 can fall into the ambiguous class. They attributed this to the

401   inhomogeneous vertical distributions of $HCHO$ and NO_2. However, there is a feature in our

402   second experiment which carries over quantitatively to the more fundamental problem which

403   is the dependence of $HCHO$ production on NO_x [Wolfe et al., 2016]. This initial finding

404   motivates us to further investigate this relationship by comparing NO_2 concentrations with the

405    $HCHO$ formation.

406   Figure 10a depicts the $HCHO$ formation isopleths for different NO_2 and VOCs

407   concentrations. At low VOC environments, the $HCHO$ formation is dampened by increasing

408   NO_2 (due to OH suppression and formation of organic nitrates), whereas at high VOC

409   conditions, the availability of RO_2 and HO_2 results in enhancing VOC oxidation (thus larger

410    $HCHO$ formation) with respect to NO_2 for given NO_2 levels (<6 ppbv). Revisiting Figure 9, at

411   a point that $HCHO = 22$ ppbv and $NO_2 = 8$ ppbv, the $LNO_x/LRO_x = 2.7$ lines suggest that this data

412   point is in NO_x-saturated while the conventional threshold ($HCHO/NO_2 = 2$) indicates

413   otherwise. According to Figure 10a, an increase in NO_2 at this point should naturally result in

414   reducing $HCHO$ formation, which in turn, moves this point to the bottom and the right side of

415   the $P(O_3)$ isopleth (i.e., toward NO_x-saturated regime). This provides theoretical evidence that

416   the hypothesis on this point being NO_x-sensitive regime (by $HCHO/NO_2 = 2$) is spurious. The

417   wide range of $HCHO/NO_2$ ratios that the transition line falls in can be partly explainable by the

418   impact of NO_2 on $HCHO$ formation. Under VOC rich environments, the feedback of NO_2 on

419   HCHO formation increases the numerator of the HCHO/NO$_2$ ratios (and denominator of
420   LNO$_x$/LRO$_x$) indicating the transition occurs at larger ratios. The inherit dependence of HCHO
421   formation on NO$_x$ concentrations have comprehensively studied in Valin et al. [2016], Marias
422   et al. [2012], and Wolfe et al. [2016]. The major driver for this chemical feedback is by OH
423   production/loss. To better demonstrate this, we plot the contour map of OH concentration from
424   the same analysis done for HCHO formation in Figure 10b. The figure shows enhanced OH
425   mainly due to RO$_2$+NO reaction for given NO$_2$ concentrations (depending on the abundance
426   of VOCs), but reduced OH afterward primary due to NO$_2$+OH reaction. Therefore, the more
427   reactive a VOC compound is, the larger NO$_x$ can boost HCHO production, thus complicating
428   the HCHO/NO$_2$ ratio. We observe the same chemical tendency by calculating the derivative of
429   HCHO columns with respect to the NO$_x$ emissions using the CMAQ Direct Decoupled Method
430   (DDM) [Cohen et al., 2005] during afternoon in May-June 2016 [Figure S10].

431   With this caveat in mind, we define our case-specific transition line for mapping
432   GeoTASO columns into the different regimes by fitting a line to the LNO$_x$/LRO$_x$=2.7 which
433   results in the following equation:

$$HCHO = 3.7 \times (NO_2 - 2.2\ ppbv) \tag{7}$$

434   It is worth pointing out here that this is for the local relationship under a well-mixed planetary
435   boundary condition, which may not translate easily to the ratio of the columns. To convert the
436   intercept to column, we assume uniformly mixed NO$_2$ concentrations (2.2 ppbv) from 0 to 2
437   km above ground level and for higher altitudes; we follow the CMAQ-WRF profiles over
438   Seoul:

$$HCHO = 3.7 \times (NO_2 - 1.14 \times 10^{16} molec.cm^{-2}) \tag{8}$$

439   **Mapping Chemical Conditions over Seoul — GeoTASO**

440   To proceed further with the link between the transition line derived from the second
441   experiment and GeoTASO HCHO/NO$_2$ columns, will first require a comparison of DC-8
442   HCHO/NO$_2$ ratios to those of GeoTASO on June 9th 2016 at 1400-1600 LST. Figure 11 shows
443   a point-to-point comparison of these two datasets collocated spatially. The temporal co-
444   registration of both datasets is not feasible; we have to assume that both datasets are exposed
445   to the same atmospheric condition in the 1400-1600 LST window. The comparison suggests
446   that DC-8 fairly captures ~60% of the variance in GeoTASO. However, GeoTASO
447   HCHO/NO$_2$ ratios tend to be higher than those of DC-8. A number of factors contribute to the
448   disagreement between two datasets: i) the accuracy in the retrievals [Nowlan et al., 2016;
449   Nowlan et al., 2018; Lamsal et al., 2017] can directly contaminate HCHO/NO$_2$ column, ii) the
450   assumption of the effective vertical diffusion mechanism within the mixed layer should not

451 rule out the impact of the free troposphere on the magnitude of column, and iii) the spatial

452 heterogeneity in the observations inevitably leads to some degree of disagreements.

453   We further use Eq.8 to classify the Seoul metropolitan area into NO_x-saturated and

454 NO_x-sensitive regimes at different times of the day (1000-1600 LST), shown in Figure 12.

455 Compared with former studies using satellite observations [Choi and Souri, 2015a,b; Jin and

456 Holloway, 2015; Duncan et al., 2010; Choi et al., 2012; Chang et al., 2016; Jin et al., 2017;

457 Souri et al., 2017], GeoTASO with unprecedented spatial and temporal resolutions provides

458 much more in-depth information at a fine scale. In a broad picture, NO_x-sensitive regimes are

459 primarily observed in suburbs, whereas the NO_x-saturated regimes are mostly confined to urban

460 settings. Areas that are located in NO_x-saturated regime change over time, shrinking from the

461 morning time to the afternoon which is mainly associated with photochemistry, although the

462 impact of meteorology and traffic patterns cannot be neglected. We constantly observe how

463 the Olympic Park (shown with a red circle) falls into NO_x-saturated regime suggesting that the

464 abrupt increase in isoprene in this area [Figure S9] can strongly enhance $P(O_3)$. Based on OMI

465 observations from 2005-2015, Jin et al. [2017] labeled Seoul as the transitional regime in warm

466 seasons. Integrating all pixels from GeoTASO leads to the same conclusion (assuming

467 $1 < HCHO/NO_2 < 2$ as the transitional class), suggesting that the broad picture of the latter

468 remains correct; however, the finer resolution of GeoTASO allows the regimes to be further

469 broken out into smaller segments, showing significant spatial variations in $HCHO/NO_2$ ratios.

470 To better demonstrate how a finer spatial resolution can be critical for our application, we chose

471 an area in Incheon by putting together the CMAQ-derived ratios in 27×27 km^2 and those of

472 GeoTASO, shown in Figure 13. By virtue of having a large portion (63%) of NO_x-saturated

473 regime observed by GeoTASO, the CMAQ model correctly labels this area as the same

474 category, but according to GeoTASO, the sub-pixel variabilities are large suggesting that high

475 resolution sensors offer a potential basis for designing more specific mitigation strategies.

476 **Summary**

477   Persistent increases in stagnation, continental background concentrations, and

478 photochemistry go hand-in-hand and lead to an ozone extreme event in the Seoul metropolitan

479 area on June 9th 2016, making this day an interesting target to study ozone sensitivity.

480 Specifically, DC-8 measurements observed mixing-layer NO_2 and HCHO concentrations up to

481 30 and 9 ppbv respectively over the city during the afternoon, which is an indication of an

482 exceptionally degraded air quality. To study ozone chemistry, we conduct an ensemble of

483 steady-state box models constrained by qualified observations within the mixing-layer (<2 km).

484 The ensemble of models suggests elevated volatile organic compound reactivity (VOCR) rates

485   (~ 8 s^{-1}) close to the Olympic Park in eastern Seoul mainly due to abundance of both isoprene

486   and NO$_x$, resulting in enhancement of net ozone production rate (P(O$_3$)) by 12 ppbv hr^{-1}. The

487   same observations are captured in Sullivan et al. [2019].

488   We further study the P(O$_3$) dependency on NO by differentiating observations in rural

489   areas (>50 km far from Seoul) and urban ones (< 50 km). In the rural areas, a strong linear

490   relationship between the two quantities is found mainly due to abundant VOCs; the relationship

491   turns into a quadratic form in the urban areas resulting from NO$_2$+OH reaction. The maxima

492   of this quadratic function occurs at a wide range of NO (1.2-2.46 ppbv) giving a strong

493   indication of the presence of diverse emissions. We extrapolate our analysis by perturbing the

494   primary compounds and find that the loss of NOx (LNO$_x$) to the loss of HO$_2$+RO$_2$ (LRO$_x$)

495   which is roughly equivalent to HNO$_3$/H$_2$O$_2$ suggested by Sillman et al. [2002] is a robust way

496   to differentiate NO$_x$-sensitive (i.e. NO$_x$-limited) or NO$_x$-saturated (i.e. VOC-limited)

497   [Schroeder et al., 2017]. Following the ratio of LNO$_x$/LRO$_x$~2.7 describing the transition line,

498   the conventional thresholds of HCHO/NO$_2$ ratios, a proxy indicator commonly applied using

499   satellite-derived observations, are not always applicable. Our theoretically observational-

500   calculational experiment indicates that NO$_2$-HCHO chemical relationship plays a major role in

501   usefulness of the mathematical formulation of HCHO/NO$_2$. Under VOC rich environment, the

502   acceleration of HCHO formation with respect to NO$_2$ suggests that the transition line occurs at

503   larger HCHO/NO$_2$ ratios (up to 4). Our analysis highlights the limitation of using the

504   HCHO/NO$_2$ ratios at pinpointing the regimes from a chemical point of view. This means that

505   the conventional approach of formulating this indicator is facing problems under VOC rich

506   environments, thereby a fundamental reformulation might be needed. We then reformulate the

507   indicator to be able to match with LNO$_x$/LRO$_x$~2.7 which leads to HCHO = 3.7×(NO$_2$ −

508   1.14×10^{16} molec.cm^{-2}). The advantage of using this mathematical format over a ratio lies in the

509   fact that it removes the need for providing a wide range of thresholds depending on VOC

510   environment, although the numbers here are calibrated locally.

511   Making use of newly available airborne remotely sensed data at unprecedented spatial

512   and temporal resolutions, we use the redesigned formula in an effort to classify the chemical

513   condition regimes over Seoul. Compared to a crude classification suggested in former studies

514   using coarse satellite observations [Souri et al., 2017; Jin et al., 2017], the Geostationary Trace

515   gas and Aerosol Sensor Optimization (GeoTASO) airborne instrument reveals more in-depth

516   spatial and temporal variabilities associated with the regimes. We observe a larger ring of NO$_x$-

517   saturated regimes at 10-12 LST compared to the afternoon possibly due to less active

518   photochemistry. The Olympic Park in which P(O$_3$) is high is constantly observed in NO$_x$-

519   saturated regime throughout the daytime. Results ensure the capability of future geostationary

520   satellites at better capturing the chemical condition regimes with much improved spatial and

521   temporal coverage.

522   **Acknowledgment**

527   **Author Contributions**

528   A.H.S designed the study, simulated the WRF-CMAQ and the box model, analyzed the data,

529   made all figures and wrote the manuscript. C.R.N retrieved HCHO columns from GeoTASO.

530   G.M.W guided the box simulations and the interpretation. L.L retrieved NO_2 columns from

531   GeoTASO. G.G and C.E.C.M helped with the retrieval and the interpretation. S.J collected the

532   GeoTASO data. A.F, D.R.B, A.W., and G.S.D measured various compounds on DC-8 used in

533   the analysis. X.L and K.C conceived and guided the interpretation. All authors contributed to

534   discussions and edited the manuscript.

535

536

References

538 Bey, I., Jacob, D.J., Yantosca, R.M., Logan, J.A., Field, B.D., Fiore, A.M., Li, Q., Liu, H.Y.,
539   Mickley, L.J. and Schultz, M.G., 2001. Global modeling of tropospheric chemistry
540   with assimilated meteorology: Model description and evaluation. Journal of
541   Geophysical Research: Atmospheres, 106(D19), pp.23073-23095.
542 Boersma, K.F., Eskes, H.J., Veefkind, J.P., Brinksma, E.J., Van Der A, R.J., Sneep, M., Van
543   Den Oord, G.H.J., Levelt, P.F., Stammes, P., Gleason, J.F. and Bucsela, E.J., 2007.
544   Near-real time retrieval of tropospheric NO 2 from OMI. Atmospheric Chemistry and
545   Physics, 7(8), pp.2103-2118.
546 Byun, D. and Schere, K.L., 2006. Review of the governing equations, computational
547   algorithms, and other components of the Models-3 Community Multiscale Air Quality
548   (CMAQ) modeling system. Applied mechanics reviews, 59(2), pp.51-77.
549 Chan Miller, C., Jacob, D.J., Marais, E.A., Yu, K., Travis, K.R., Kim, P.S., Fisher, J.A., Zhu,
550   L., Wolfe, G.M., Hanisco, T.F. and Keutsch, F.N., 2017. Glyoxal yield from isoprene
551   oxidation and relation to formaldehyde: chemical mechanism, constraints from
552   SENEX aircraft observations, and interpretation of OMI satellite data. Atmospheric
553   Chemistry and Physics, 17(14), pp.8725-8738.
554 Chance, K., 2001. OMI algorithm theoretical basis document. volume IV: OMI trace gas
555   algorithms, https://ozoneaq.gsfc.nasa.gov/media/docs/ATBD-OMI-04.pdf
556 Chance, K., 2001. OMI algorithm theoretical basis document. volume IV: OMI trace gas
557   algorithms, https://ozoneaq.gsfc.nasa.gov/media/docs/ATBD-OMI-04.pdf
558 Chance, K., J.P. Burrows, and W. Schneider, 1991. Retrieval and molecule sensitivity studies
559   for the Global Ozone Monitoring Experiment and the Scanning Imaging Absorption
560   spectroMeter for Atmospheric CHartograpHY. Proc. S.P.I.E., 1491, 151-165,
561   doi:10.1117/12.46657.
562 Chance, K., J.P. Burrows, D. Perner, and W. Schneider, 1997. Satellite measurements of
563   atmospheric ozone profiles, including tropospheric ozone, from ultraviolet/visible
564   measurements in the nadir geometry: a potential method to retrieve tropospheric
565   ozone. J. Quant. Spectrosc. Radiat. Transfer, 57, 467-476, doi:10.1016/S0022-
566   4073(96)00157-4.
567 Chance, K., P. Palmer, and R. Spurr, 2000. Satellite observations of formaldehyde over North
568   America. Geophys. Res. Lett., 27(21), 3461–3464.
569 Chance, K., X. Liu, C. Chan Miller, G.González Abad, G. Huang, C. Nowlan, A. Souri, R.
570   Suleiman, K. Sun, H. Wang, L. Zhu, P. Zoogman, J. Al-Saadi, J.-C. Antuña-Marrero,
571   J. Carr, R. Chatfield, M. Chin, R. Cohen, D. Edwards, J. Fishman, D. Flittner, J.
572   Geddes, M. Grutter, J.R. Herman, D.J. Jacob, S. Janz J. Joiner, J. Kim, N.A. Krotkov,
573   B. Lefer, R.V. Martin, O.L. Mayol-Bracero, A. Naeger, M. Newchurch, G.G. Pfister,
574   K. Pickering, R.B. Pierce, C. Rivera Cárdenas, A. Saiz-Lopez, W. Simpson, E. Spinei,
575   R.J.D. Spurr, J.J. Szykman, O. Torres, and J. Wang, TEMPO Green Paper: Chemistry,
576   physics, and meteorology experiments with the Tropospheric Emissions: Monitoring
577   of Pollution instrument, Proc. SPIE, In Sensors, Systems, and Next-Generation
578   Satellites XXIII (Vol. 11151, p. 111510B). International Society for Optics and
579   Photonics.
580 Chang, C.Y., Faust, E., Hou, X., Lee, P., Kim, H.C., Hedquist, B.C. and Liao, K.J., 2016.
581   Investigating ambient ozone formation regimes in neighboring cities of shale plays in
582   the Northeast United States using photochemical modeling and satellite retrievals.
583   Atmospheric environment, 142, pp.152-170.
584 Chen, F. and Dudhia, J., 2001. Coupling an advanced land surface–hydrology model with the

585   Penn State–NCAR MM5 modeling system. Part I: Model implementation and
586   sensitivity. Monthly Weather Review, 129(4), pp.569-585.
587 Choi, Y. and Souri, A.H., 2015a. Chemical condition and surface ozone in large cities of
588   Texas during the last decade: Observational evidence from OMI, CAMS, and model
589   analysis. Remote Sensing of Environment, 168, pp.90-101.
590 Choi, Y. and Souri, A.H., 2015b. Seasonal behavior and long-term trends of tropospheric
591   ozone, its precursors and chemical conditions over Iran: A view from space.
592   Atmospheric Environment, 106, pp.232-240.
593 Choi, Y., Kim, H., Tong, D. and Lee, P., 2012. Summertime weekly cycles of observed and
594   modeled NO x and O 3 concentrations as a function of satellite-derived ozone
595   production sensitivity and land use types over the Continental United States.
596   Atmospheric Chemistry and Physics, 12(14), pp.6291-6307.
597 Cohan, D.S., Hakami, A., Hu, Y. and Russell, A.G., 2005. Nonlinear response of ozone to
598   emissions: Source apportionment and sensitivity analysis. Environmental Science &
599   Technology, 39(17), pp.6739-6748.
600 Cooper, O.R., Parrish, D.D., Ziemke, J., Balashov, N.V., Cupeiro, M., Galbally, I.E., Gilge,
601   S., Horowitz, L., Jensen, N.R., Lamarque, J.F. and Naik, V., 2014. Global distribution
602   and trends of tropospheric ozone: An observation-based review. Elem Sci Anth, 2.
603 De Smedt, I., Stavrakou, T., Hendrick, F., Danckaert, T., Vlemmix, T., Pinardi, G., Theys,
604   N., Lerot, C., Gielen, C., Vigouroux, C. and Hermans, C., 2015. Diurnal, seasonal and
605   long-term variations of global formaldehyde columns inferred from combined OMI
606   and GOME-2 observations. Atmospheric Chemistry & Physics, 15(8).
607 Duncan, B.N., Yoshida, Y., Olson, J.R., Sillman, S., Martin, R.V., Lamsal, L., Hu, Y.,
608   Pickering, K.E., Retscher, C., Allen, D.J. and Crawford, J.H., 2010. Application of
609   OMI observations to a space-based indicator of NOx and VOC controls on surface
610   ozone formation. Atmospheric Environment, 44(18), pp.2213-2223.
611 Goldberg, D. L., Saide, P. E., Lamsal, L. N., Foy, B. d., Lu, Z., Woo, J.-H., Kim, Y., Kim, J.,
612   Gao, M., Carmichael, G., and Streets, D. G.: A top-down assessment using OMI NO2
613   suggests an underestimate in the NOx emissions inventory in Seoul, South Korea,
614   during KORUSAQ, Atmos. Chem. Phys., 19, 1801–1818,
615 González Abad G., Souri, A.H., Bak, J., Chance, K., Flynn, L.E., Krotkov, N.A., Lamsal, L.,
616   Li, C., Liu, X., Miller, C.C. and Nowlan, C.R., 2019. Five decades observing Earth's
617   atmospheric trace gases using ultraviolet and visible backscatter solar radiation from
618   space. Journal of Quantitative Spectroscopy and Radiative Transfer.
619 González Abad, G., Liu, X., Chance, K., Wang, H., Kurosu, T.P. and Suleiman, R., 2015.
620   Updated Smithsonian Astrophysical Observatory Ozone Monitoring Instrument (SAO
621   OMI) formaldehyde retrieval. Atmospheric Measurement Techniques, 8(1), pp.19-32.
622 Guenther, A., Karl, T., Harley, P., Wiedinmyer, C., Palmer, P.I. and Geron, C., 2006.
623   Estimates of global terrestrial isoprene emissions using MEGAN (Model of Emissions
624   of Gases and Aerosols from Nature). Atmospheric Chemistry and Physics, 6(11),
625   pp.3181-3210.
626 Herman, J., Spinei, E., Fried, A., Kim, J., Kim, J., Kim, W., Cede, A., Abuhassan, N. and
627   Segal Rozenhaimer, M., 2018. NO2 and HCHO measurements in Korea from 2012 to
628   2016 from Pandora spectrometer instruments compared with OMI retrievals and with
629   aircraft measurements during the KORUS-AQ campaign. Atmospheric Measurement
630   Techniques, 11(8), pp.4583-4603.
631 Hildebrandt Ruiz, L. and Yarwood, G., 2013. Interactions between Organic Aerosol and
632   NOy: Influence on Oxidant Production, Final report for AQRP project 12-
633   012. Prepared for the Texas Air Quality Research Program.
634 Hong, S.Y. and Lim, J.O.J., 2006. The WRF single-moment 6-class microphysics scheme

635   (WSM6). Asia-Pacific Journal of Atmospheric Sciences, 42(2), pp.129-151.

636 Ingmann, P., Veihelmann, B., Langen, J., Lamarre, D., Stark, H. and Courrèges-Lacoste,
637   G.B., 2012. Requirements for the GMES Atmosphere Service and ESA's
638   implementation concept: Sentinels-4/-5 and-5p. Remote Sensing of Environment,
639   120, pp.58-69.

640 Jeon, W., Choi, Y., Souri, A.H., Roy, A., Diao, L., Pan, S., Lee, H.W. and Lee, S.H., 2018.
641   Identification of chemical fingerprints in long-range transport of burning induced
642   upper tropospheric ozone from Colorado to the North Atlantic Ocean. Science of The
643   Total Environment, 613, pp.820-828.

644 Jin, X. and Holloway, T., 2015. Spatial and temporal variability of ozone sensitivity over
645   China observed from the Ozone Monitoring Instrument. Journal of Geophysical
646   Research: Atmospheres, 120(14), pp.7229-7246.

647 Jin, X., Fiore, A.M., Murray, L.T., Valin, L.C., Lamsal, L.N., Duncan, B., Folkert Boersma,
648   K., De Smedt, I., Abad, G.G., Chance, K. and Tonnesen, G.S., 2017. Evaluating a
649   space-based indicator of surface ozone-NOx-VOC sensitivity over midlatitude source
650   regions and application to decadal trends. Journal of Geophysical Research:
651   Atmospheres, 122(19), pp.10-439.

652 Kain, J.S., 2004. The Kain–Fritsch convective parameterization: an update. Journal of applied
653   meteorology, 43(1), pp.170-181.

654 Ke, Y., Leung, L.R., Huang, M., Coleman, A.M., Li, H. and Wigmosta, M.S., 2012.
655   Development of high resolution land surface parameters for the Community Land
656   Model. Geoscientific Model Development, 5(6), pp.1341-1362.

657 Kim, J., et al., New Era of Air Quality Monitoring from Space: Geostationary Environment
658   Monitoring Spectrometer (GEMS), Bull. Amer. Meteor. Soc.,
659   https://doi.org/10.1175/BAMS-D-18-0013.1.

660 Kim, S., Jeong, D., Sanchez, D., Wang, M., Seco, R., Blake, D., Meinardi, S., Barletta, B.,
661   Hughes, S., Jung, J. and Kim, D., 2018. The controlling factors of photochemical
662   ozone production in Seoul, South Korea. Aerosol and Air Quality Research, 18(9),
663   pp.2253-2261.

664 Kleinman, L.I., Daum, P.H., Lee, Y.N., Nunnermacker, L.J., Springston, S.R., Weinstein-
665   Lloyd, J. and Rudolph, J., 2002. Ozone production efficiency in an urban area. Journal
666   of Geophysical Research: Atmospheres, 107(D23), pp.ACH-23.

667 Lamsal, L.N., Janz, S.J., Krotkov, N.A., Pickering, K.E., Spurr, R.J.D., Kowalewski, M.G.,
668   Loughner, C.P., Crawford, J.H., Swartz, W.H. and Herman, J.R., 2017. High-
669   resolution NO2 observations from the Airborne Compact Atmospheric Mapper:
670   Retrieval and validation. Journal of Geophysical Research: Atmospheres, 122(3),
671   pp.1953-1970.

672 Leitch, J.W., T. Delker, W. Good, L. Ruppert, F. Murcray, K. Chance, X. Liu, C. Nowlan, S.
673   J. Janz, N. A. Krotkov, K. E. Pickering, M. Kowalewski, J. Wang, 2014, The
674   GeoTASO airborne spectrometer project, Proc. SPIE 9218, Earth Observing Systems
675   XIX, 92181H, doi: 10.1117/12.206376.

676 Li, M., Zhang, Q., Kurokawa, J.I., Woo, J.H., He, K.B., Lu, Z., Ohara, T., Song, Y., Streets,
677   D.G., Carmichael, G.R. and Cheng, Y.F., 2015. MIX: a mosaic Asian anthropogenic
678   emission inventory for the MICS-Asia and the HTAP projects. Atmos. Chem. Phys.
679   Discuss, 15(23), pp.34813-34869.

680 Mao, J., Ren, X., Chen, S., Brune, W.H., Chen, Z., Martinez, M., Harder, H., Lefer, B.,
681   Rappenglueck, B., Flynn, J. and Leuchner, M., 2010. Atmospheric oxidation capacity
682   in the summer of Houston 2006: Comparison with summer measurements in other
683   metropolitan studies. Atmospheric Environment, 44(33), pp.4107-4115.

684 Marais, E.A., Jacob, D.J., Kurosu, T.P., Chance, K., Murphy, J.G., Reeves, C., Mills, G.,

Casadio, S., Millet, D.B., Barkley, M.P. and Paulot, F., 2012. Isoprene emissions in Africa inferred from OMI observations of formaldehyde columns. Atmospheric Chemistry and Physics, 12(14), pp.6219-6235.

Marchenko S., N.A. Krotkov, L.N. Lamsal, E.A. Celarier, W.H. Swartz, E.J. Bucsela, Revising the slant- column density retrieval of nitrogen dioxide observed by the Ozone Monitoring Instrument, J. Geophys. Res., DOI: 10.1002/2014JD022913, 2015.

Martin, R.V., Fiore, A.M. and Van Donkelaar, A., 2004. Space-based diagnosis of surface ozone sensitivity to anthropogenic emissions. Geophysical Research Letters, 31(6).

Mencaraglia, F., Bianchini, G., Boscaleri, A., Carli, B., Ceccherini, S., Raspollini, P., Perrin, A. and Flaud, J.M., 2006. Validation of MIPAS satellite measurements of HNO3 using comparison of rotational and vibrational spectroscopy. Journal of Geophysical Research: Atmospheres, 111(D19).

Nowlan, C.R., Liu, X., Janz, S.J., Kowalewski, M.G., Chance, K., Follette-Cook, M.B., Fried, A., González Abad, G., Herman, J.R., Judd, L.M. and Kwon, H.A., 2018. Nitrogen dioxide and formaldehyde measurements from the GEOstationary Coastal and Air Pollution Events (GEO-CAPE) Airborne Simulator over Houston, Texas. Atmospheric Measurement Techniques, 11(11), pp.5941-5964.

Nowlan, C.R., Liu, X., Leitch, J.W., Chance, K., González Abad, G., Liu, C., Zoogman, P., Cole, J., Delker, T., Good, W. and Murcray, F., 2016. Nitrogen dioxide observations from the Geostationary Trace gas and Aerosol Sensor Optimization (GeoTASO) airborne instrument: Retrieval algorithm and measurements during DISCOVER-AQ Texas 2013. Atmospheric Measurement Techniques, 9(6), pp.2647-2668.

Pan, S., Choi, Y., Jeon, W., Roy, A., Westenbarger, D.A. and Kim, H.C., 2017. Impact of high-resolution sea surface temperature, emission spikes and wind on simulated surface ozone in Houston, Texas during a high ozone episode. Atmospheric environment, 152, pp.362-376.

Pleim, J.E., 2007. A combined local and nonlocal closure model for the atmospheric boundary layer. Part I: Model description and testing. Journal of Applied Meteorology and Climatology, 46(9), pp.1383-1395.

Pusede, S.E., Steiner, A.L. and Cohen, R.C., 2015. Temperature and recent trends in the chemistry of continental surface ozone. Chemical reviews, 115(10), pp.3898-3918.

Rinsland, C.P., Coheur, P.F., Herbin, H., Clerbaux, C., Boone, C., Bernath, P. and Chiou, L.S., 2007. Detection of elevated tropospheric hydrogen peroxide (H2O2) mixing ratios in atmospheric chemistry experiment (ACE) subtropical infrared solar occultation spectra. Journal of Quantitative Spectroscopy and Radiative Transfer, 107(2), pp.340-348.

Schaaf, C. B., Z. Wang and A. H. Strahler, Commentary on Wang and Zender-MODIS snow albedo bias at high solar zenith angles relative to theory and to in situ observations in Greenland, Rem. Sen. Env., 115, 1296-1300, 2011.

Schroeder, J.R., Crawford, J.H., Fried, A., Walega, J., Weinheimer, A., Wisthaler, A., Müller, M., Mikoviny, T., Chen, G., Shook, M. and Blake, D.R., 2017. New insights into the column CH2O/NO2 ratio as an indicator of near-surface ozone sensitivity. Journal of Geophysical Research: Atmospheres, 122(16), pp.8885-8907.

Seinfeld, J.H. and Pandis, S.N., 2016. Atmospheric chemistry and physics: from air pollution to climate change. John Wiley & Sons.

Sillman, S. and He, D., 2002. Some theoretical results concerning O3-NOx-VOC chemistry and NOx-VOC indicators. Journal of Geophysical Research: Atmospheres, 107(D22), pp.ACH-26.

Sillman, S., 1999. The relation between ozone, NOx and hydrocarbons in urban and polluted rural environments. Atmospheric Environment, 33(12), pp.1821-1845.

735 Skamarock, W.C., Klemp, J.B., Dudhia, J., Gill, D.O., Barker, D.M., Wang, W. and Powers,
736   J.G., 2005. A description of the advanced research WRF version 2 (No. NCAR/TN-
737   468+ STR). National Center For Atmospheric Research Boulder Co Mesoscale and
738   Microscale Meteorology Div.
739 Song, S.K., Shon, Z.H., Kang, Y.H., Kim, K.H., Han, S.B., Kang, M., Bang, J.H. and Oh, I.,
740   2019. Source apportionment of VOCs and their impact on air quality and health in the
741   megacity of Seoul. Environmental pollution, 247, pp.763-774.
742 Souri, A.H., Choi, Y., Jeon, W., Woo, J.H., Zhang, Q. and Kurokawa, J.I., 2017a. Remote
743   sensing evidence of decadal changes in major tropospheric ozone precursors over East
744   Asia. Journal of Geophysical Research: Atmospheres, 122(4), pp.2474-2492.
745 Souri, A.H., Choi, Y., Pan, S., Curci, G., Nowlan, C.R., Janz, S.J., Kowalewski, M.G., Liu,
746   J., Herman, J.R. and Weinheimer, A.J., 2018. First Top-Down Estimates of
747   Anthropogenic NOx Emissions Using High-Resolution Airborne Remote Sensing
748   Observations. Journal of Geophysical Research: Atmospheres, 123(6), pp.3269-3284.
749 Sullivan, J.T., McGee, T.J., Stauffer, R.M., Thompson, A.M., Weinheimer, A., Knote, C.,
750   Janz, S., Wisthaler, A., Long, R., Szykman, J. and Park, J., 2019. Taehwa Research
751   Forest: a receptor site for severe domestic pollution events in Korea during 2016.
752   Atmospheric Chemistry and Physics, 19(7), pp.5051-5067.
753 Thornton, J.A., Wooldridge, P.J., Cohen, R.C., Martinez, M., Harder, H., Brune, W.H.,
754   Williams, E.J., Roberts, J.M., Fehsenfeld, F.C., Hall, S.R. and Shetter, R.E., 2002.
755   Ozone production rates as a function of NOx abundances and HOx production rates in
756   the Nashville urban plume. Journal of Geophysical Research: Atmospheres,
757   107(D12), pp.ACH-7.
758 Tonnesen, G.S. and Dennis, R.L., 2000. Analysis of radical propagation efficiency to assess
759   ozone sensitivity to hydrocarbons and NO x: 1. Local indicators of instantaneous odd
760   oxygen production sensitivity. Journal of Geophysical Research: Atmospheres,
761   105(D7), pp.9213-9225.
762 Valin, L.C., Fiore, A.M., Chance, K. and González Abad, G., 2016. The role of OH
763   production in interpreting the variability of CH2O columns in the southeast
764   US. Journal of Geophysical Research: Atmospheres, 121(1), pp.478-493.
765 Wiedinmyer, C., Akagi, S.K., Yokelson, R.J., Emmons, L.K., Al-Saadi, J.A., Orlando, J.J.
766   and Soja, A.J., 2011. The Fire INventory from NCAR (FINN): A high resolution
767   global model to estimate the emissions from open burning. Geoscientific Model
768   Development, 4(3), p.625.
769 Wolfe, G.M., Kaiser, J., Hanisco, T.F., Keutsch, F.N., de Gouw, J.A., Gilman, J.B., Graus,
770   M., Hatch, C.D., Holloway, J., Horowitz, L.W. and Lee, B.H., 2016. Formaldehyde
771   production from isoprene oxidation across NOx regimes. Atmospheric Chemistry &
772   Physics, 16, pp. 2597–2610 .
773 Wolfe, G.M., Marvin, M.R., Roberts, S.J., Travis, K.R. and Liao, J., 2016. The framework
774   for 0-D atmospheric modeling (F0AM) v3. 1. Geoscientific Model
775   Development, 9(9), pp.3309-3319.
776 Zhu, L., Jacob, D.J., Keutsch, F.N., Mickley, L.J., Scheffe, R., Strum, M., González Abad,
777   G., Chance, K., Yang, K., Rappenglück, B. and Millet, D.B., 2017. Formaldehyde
778   (HCHO) as a hazardous air pollutant: Mapping surface air concentrations from
779   satellite and inferring cancer risks in the United States. Environmental science &
780   technology, 51(10), pp.5650-5657.
781 Zhu, L., Jacob, D.J., Mickley, L.J., Marais, E.A., Cohan, D.S., Yoshida, Y., Duncan, B.N.,
782   Abad, G.G. and Chance, K.V., 2014. Anthropogenic emissions of highly reactive
783   volatile organic compounds in eastern Texas inferred from oversampling of satellite
784   (OMI) measurements of HCHO columns. Environmental Research Letters, 9(11),

785   p.114004.

786 Zoogman, P., Liu, X., Suleiman, R.M., Pennington, W.F., Flittner, D.E., Al-Saadi, J.A.,

787   Hilton, B.B., Nicks, D.K., Newchurch, M.J., Carr, J.L. and Janz, S.J. et al., 2017.

788   Tropospheric emissions: Monitoring of pollution (TEMPO). J. Quant. Spectro. &

789   Radiat. Transfer, 186, 17-39, doi:org/10.1016/j.jqsrt.2016.05.008.

790

791

792

793 Tables

794   **Table1.** The box model configurations and inputs.

Time Steps	30 mins
Number of Solar cycles	5
Dilution constant	$1/86400$ (s^{-1})
Meteorological Inputs	Pressure, Temperature, Relative Humidity
Photolysis frequencies	Measured by NCAR's CCD Actinic Flux Spectroradiometers
Chemical Levels (Instrument#*, Precision) used for constraining the box model	H_2(1,5%), O_3(2,10%), CO (4,2%), H_2O_2 (5,30%), HNO_3 (5,30%), NO_2 (2,30%), SO_2 (6,30%) , CH_4 (4,0.1%), PAN (6,20%), Alkyl nitrates (10,10%), Isoprene (1,5%), Monoterpene (9,33%), HCHO (7,3.3%), Acetone (9,3%), Ethene (1,5%), Ethyne (1,5%), Ethane (1,5%), Methanol (9,3%), CHOCHO (8,15%), Propane (1,5%), Benzene (1,5%), Xylene (1,5%), Toluene (1,5%), Acetaldehyde (9,8%)
Chemical Levels (Instrument#*, Precision) used only for initializing the box model	OH (3,32%), HO_2 (3,32%), NO (2,20%)
Chemical Mechanism	CB6r2

795

796 * (1) UC Irvine's Whole Air Sampler (WAS), (2) NCAR 4-Channel Chemiluminescence, (3)
797 Penn State's Airborne Tropospheric Hydrogen Oxides Sensor (ATHOS), (4) NASA Langley's
798 Diode laser spectrometer, (5) Caltech's single mass analyzer, (6) Georgia Tech's ionization
799 mass spectrometer, (7) The University of Colorado at Boulder's the Compact Atmospheric
800 Multi-species Spectrometer (CAMS), (8) Korean Airborne Cavity Enhances Spectrometer, (9)
801 University of Oslo's PTR-TOF-MS instrument, and (10) University of California, Berkeley's
802 TD-LIF.

803

804
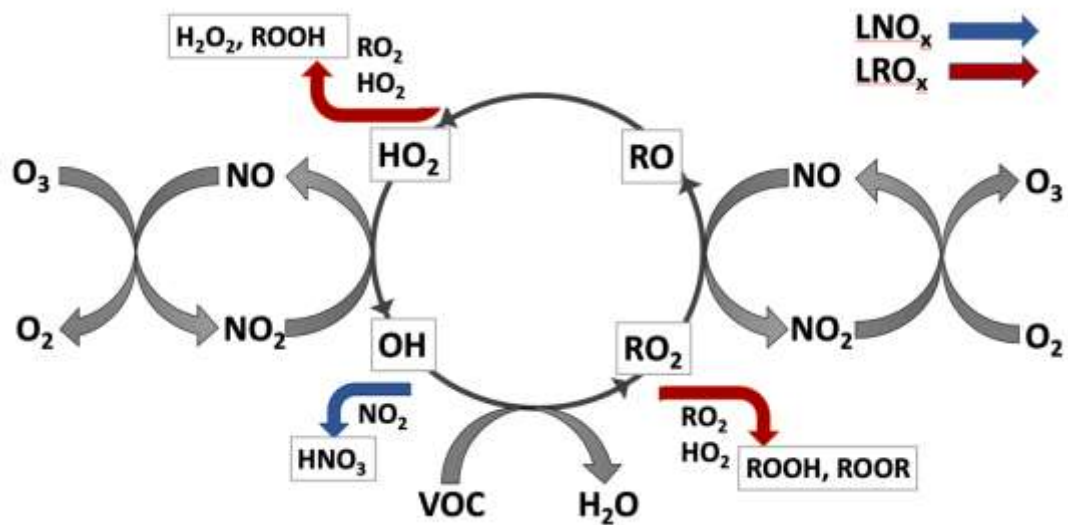
Figures:

Figure 1. A representation of the important interactions in the daytime chemistry of the
tropospheric ozone formation.

Figure 2. The location of CMAQ 27 km domain which covers China, Japan, India, South

Korea, Taiwan and some portions of Russia and South Asia.

814
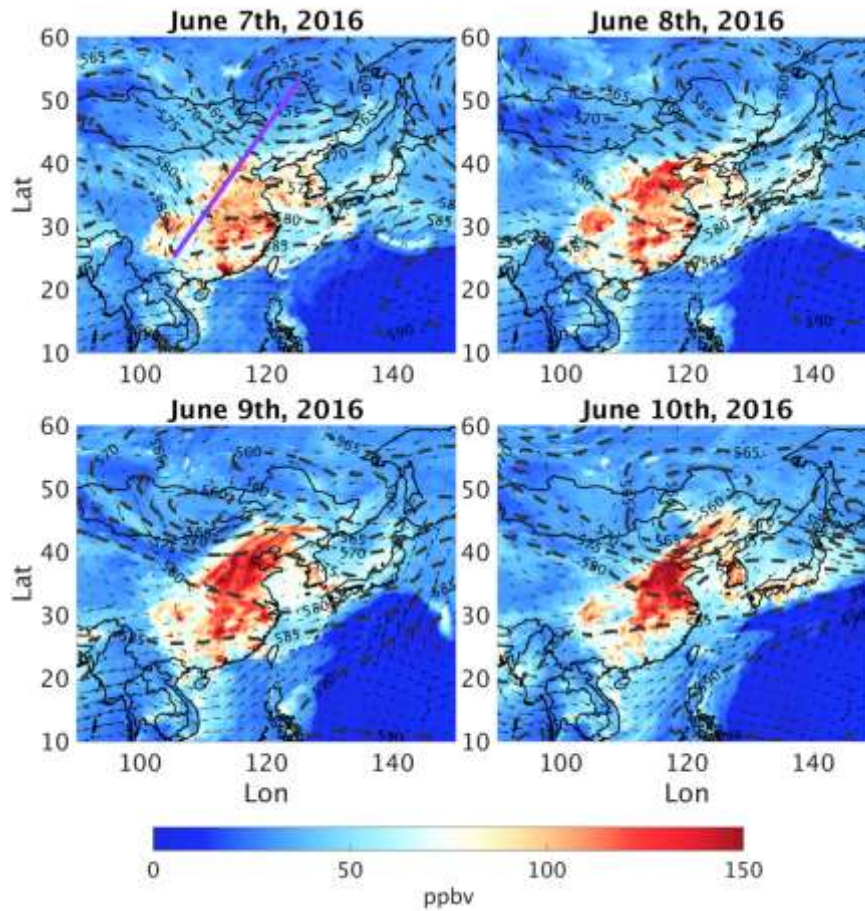
Figure 3. Synoptic-scale atmospheric conditions for East Asia at 0600 UTC on four different

days (June 7th-10th 2016). The background color indicates surface ozone mixing ratios (ppbv)

simulated by the WRF-CMAQ model. Black dashed lines represent 500 hPa geopotential

heights (decameters), and the black vectors show 700 hPa winds.
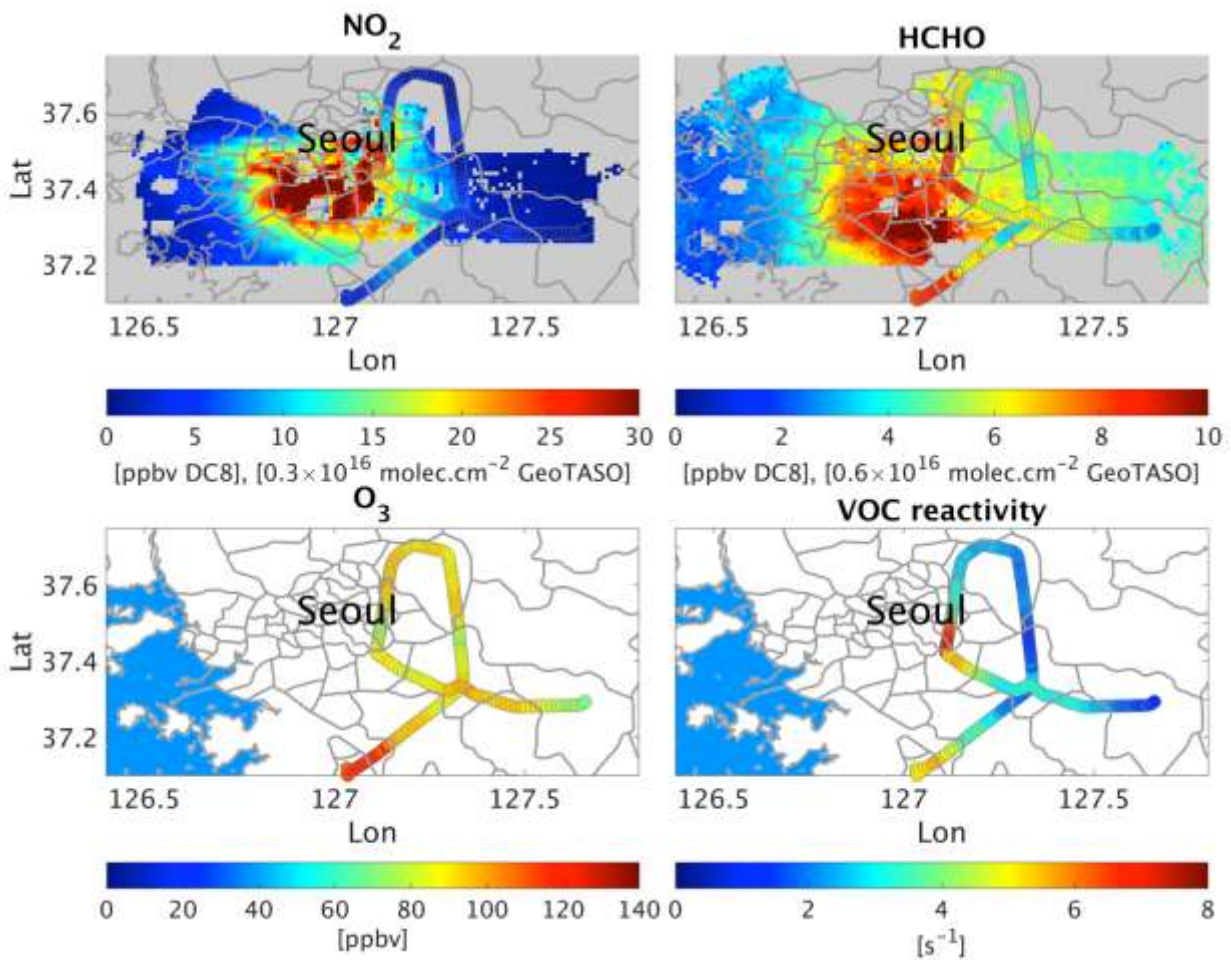
Figure 4. Contour maps of GeoTASO NO_2 and HCHO columns overlapped with DC-8 measurements on June 9th 2016 afternoon (1400-1600 LST) (first row). The measured O_3 levels and simulated VOCR based on the ensemble of box models (second row). For inferring the columns, a factor provided in captions should be applied to the colorbar values.

825
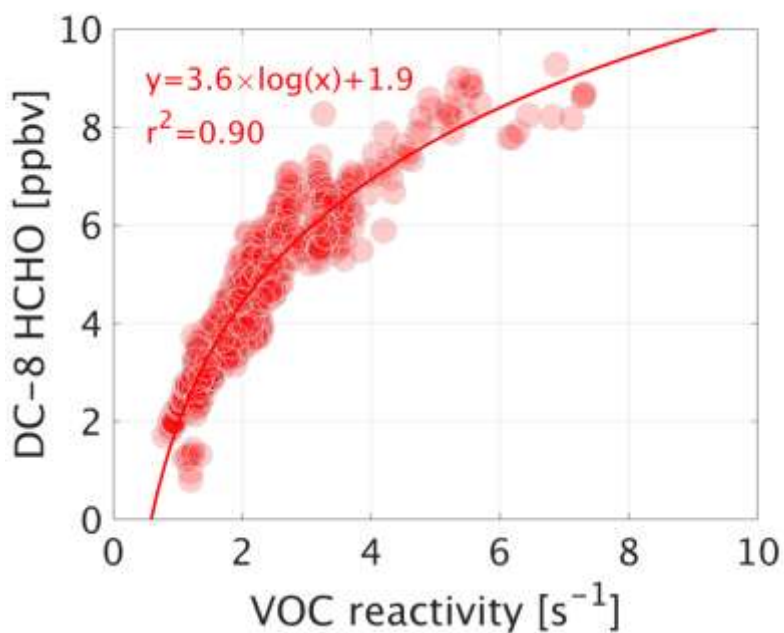
Figure 5. Point-to-point comparison of simulated VOCR rates using the constrained ensemble
of box models with measured HCHO values on June 9th 2016 afternoon (1400-1600 LST). Only
observations with less than a 2 km altitude are considered in the analysis. The black line denotes
the identity line.

830

831
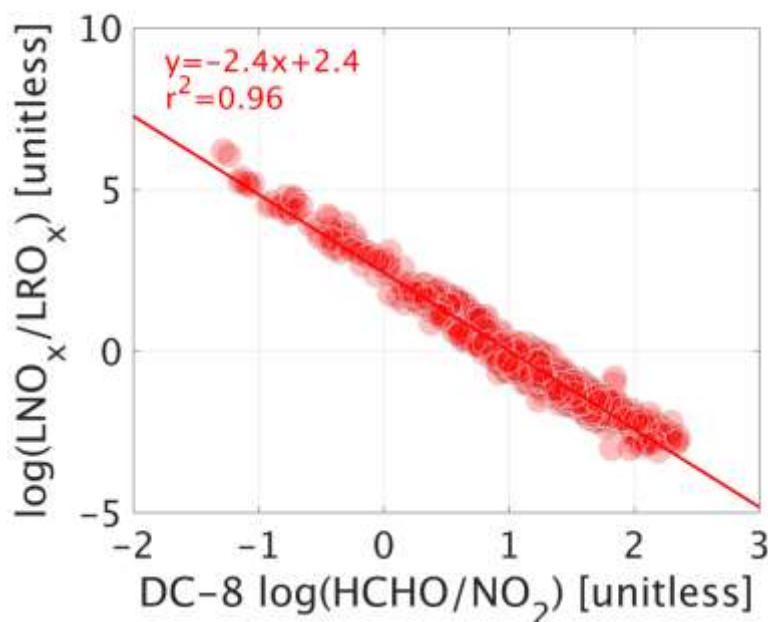
Figure 6. Point-to-point comparison of the logarithm-transformed DC-8 HCHO/NO_2 ratios vs
simulated LNO_x/LRO_x values using the constrained ensemble of box models on June 9th 2016
afternoon (1400-1600 LST). Only observations with less than a 2 km altitude (mixing layer) are
considered in the analysis.

836

837
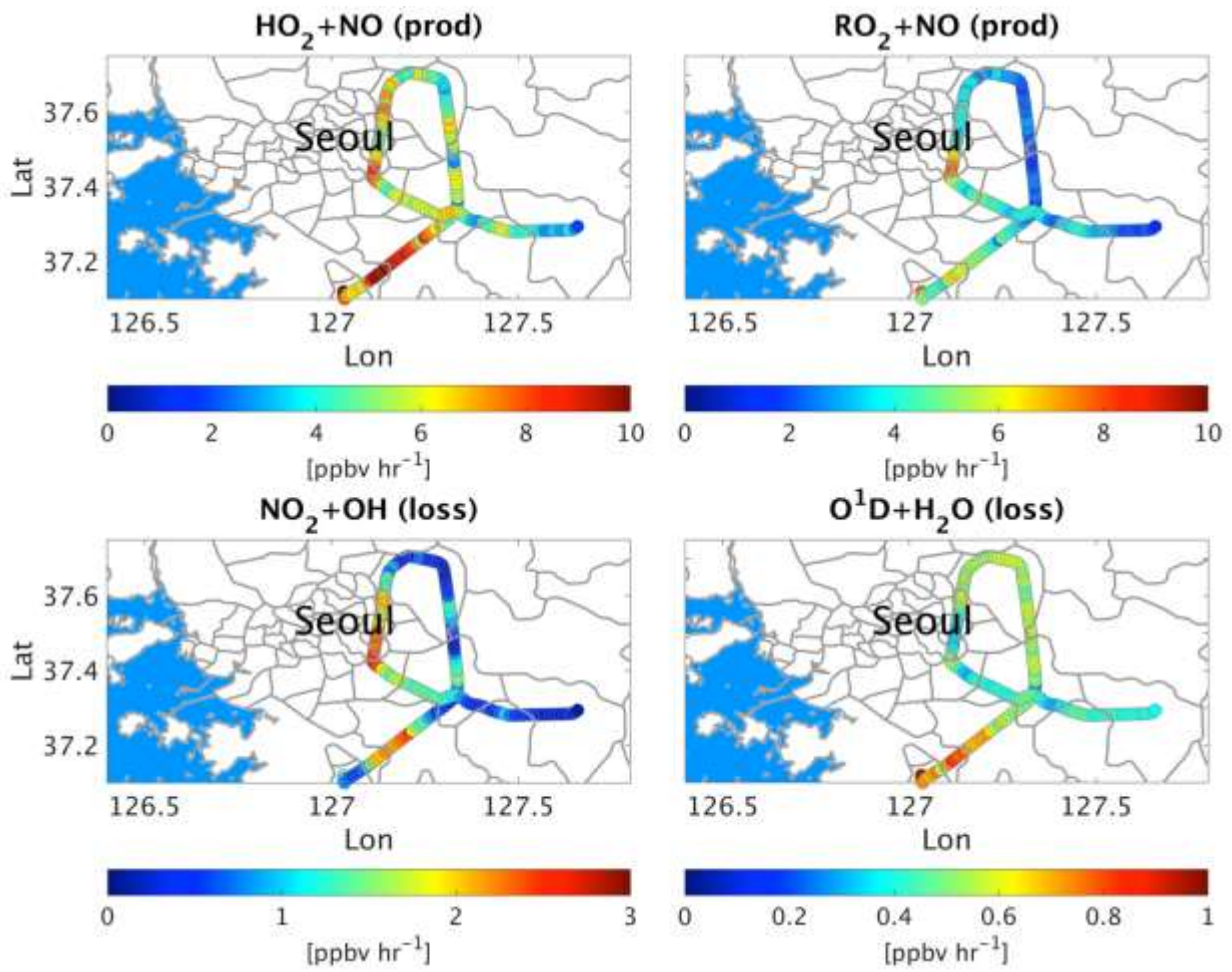
Figure 7. The simulated major pathways of photochemical ozone production (first row) and

loss (second row).

840
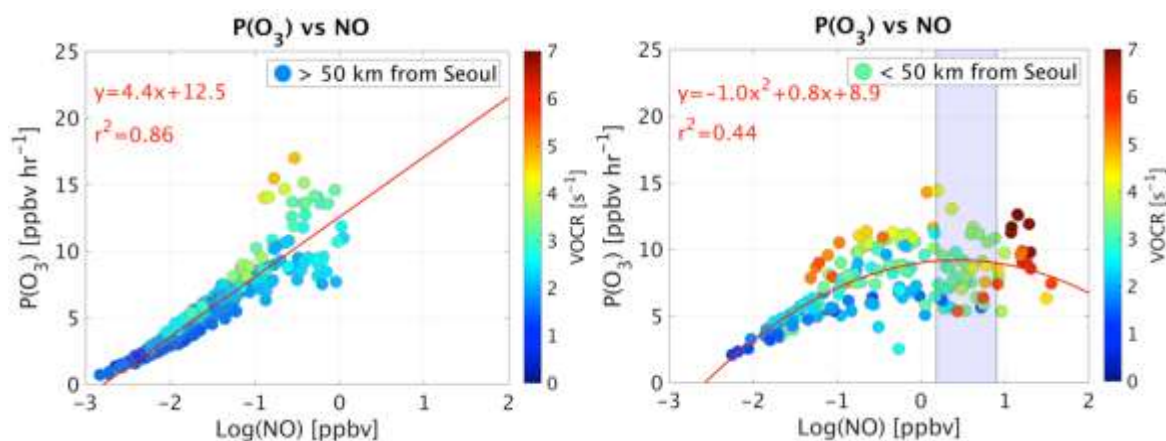
Figure 8. The relationship between observed NO and simulated P(O₃) using the constrained ensemble of box models for different regions (>50 km from Seoul in the left panel and <50 km in the right). The shade area in the right panel indicates the range of location that local maxima may fall in (at 95% confidence level).
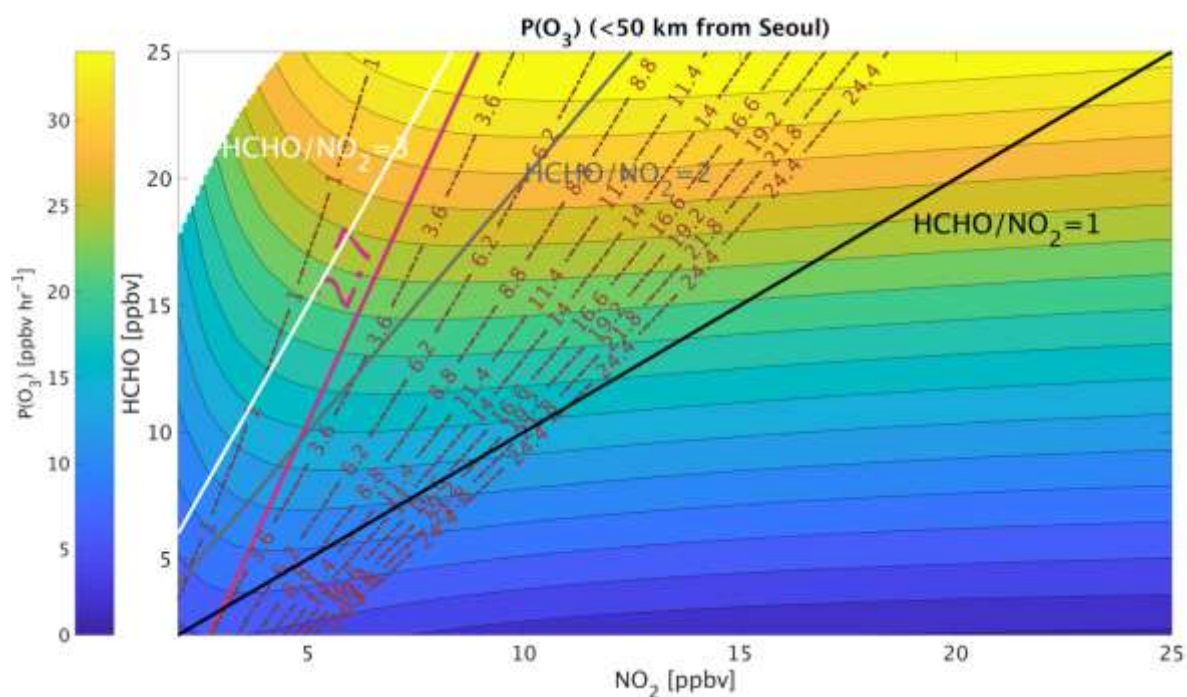
Figure 9. The P(O₃) isopleths as a function of NO₂ and HCHO concentrations overlaid by the LNOₓ/LROₓ contours (purple lines). Data points used for this plot are generated by perturbing NOₓ and primary VOCs (excluding HCHO and aromatic VOCs) using the box model described in Table 1. The data are collected from DC-8 on June 9th 2016 afternoon (1400-1600 LST).

853
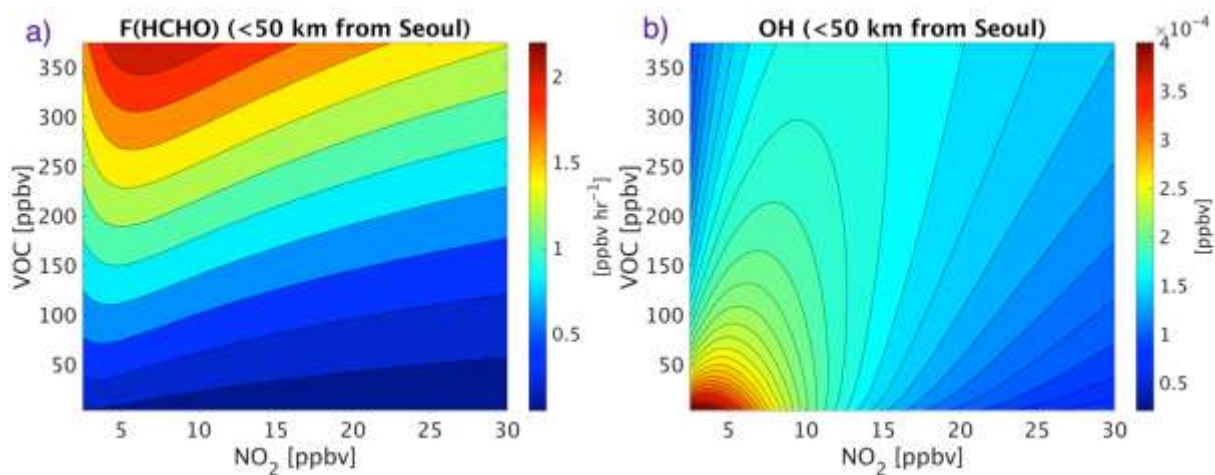
Figure 10. (a) The HCHO production isopleths, and (b) the OH concentrations isopleth as a
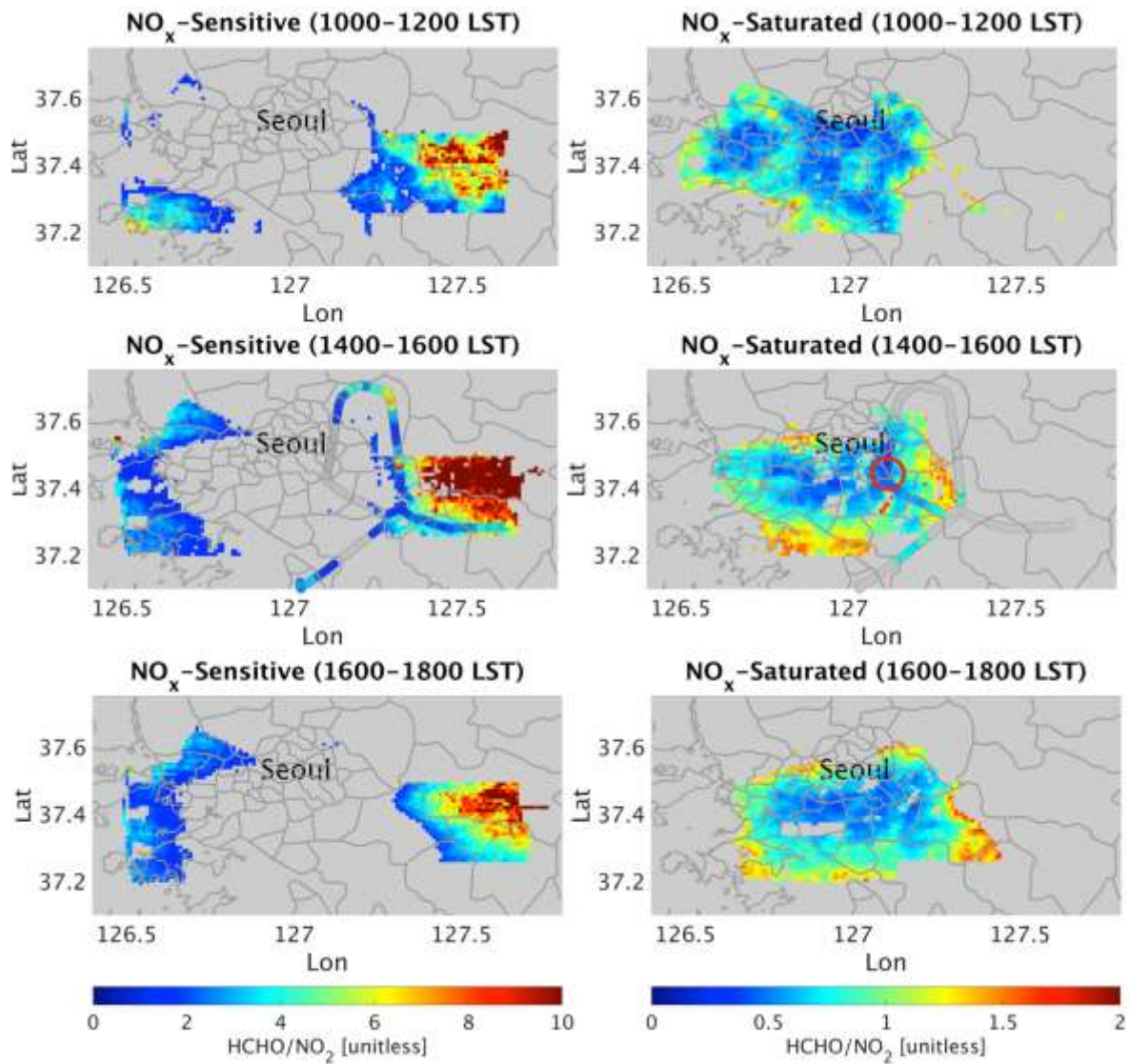function of NO_2 and VOC concentrations.

856
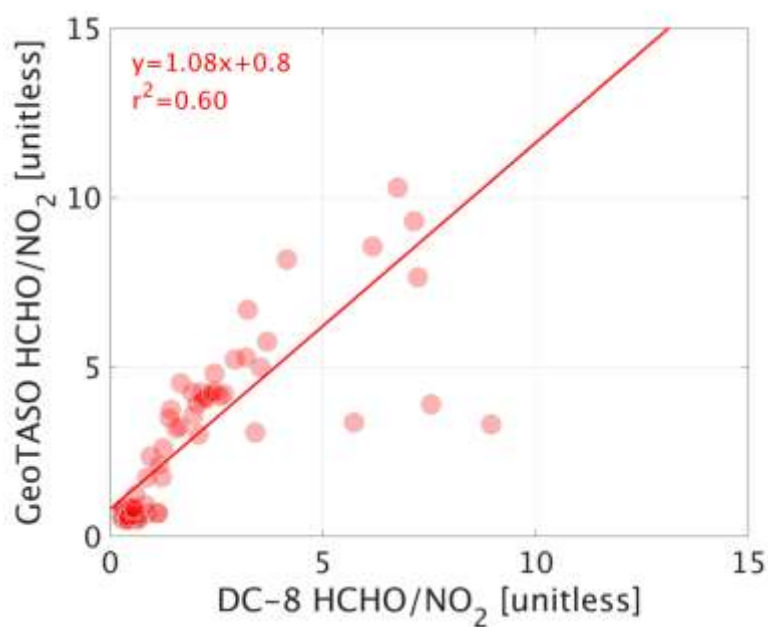
Figure 11. The comparison of GeoTASO $HCHO/NO_2$ ratios versus those of DC-8.
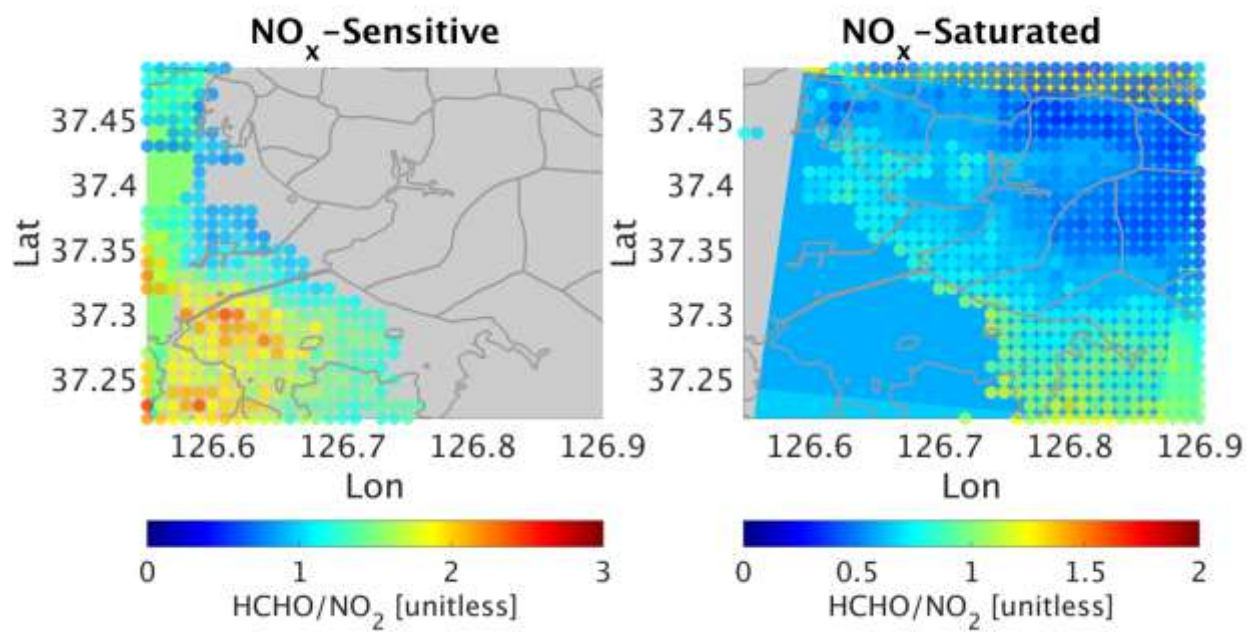
858

859

31

860

861

Figure 12. The contour maps of GeoTASO HCHO/NO$_2$ ratios labeled into two different chemical conditions regimes based on the transition line derived from this study. The observations are collected on June 9th 2016. The red circle shows the location of Olympic Park.

868

869

Figure 13. The spatial representation of HCHO/NO₂ ratios of CMAQ (background) overlaid
by those of GeoTASO for an area in Incheon, South Korea.

872